

Amethyst A. Johnson  
University of Leeds, UK

## 1. INTRODUCTION

Tropical cyclone asymmetry can be determined by many environmental factors, such as the presence of deep layer vertical wind shear (e.g. Corbosiero & Molinari 2002, 2003, Uhlhorn et al. 2014, Shimada et al. 2024) and landfall (e.g. Chan & Liang 2003, Chen & Yau 2003, Hlywiak & Nolan 2022, Rogers & Zhang 2023). Tropical Cyclone Veronica (2019) exhibited an asymmetric wind field during landfall which was not consistent with the typical landfall-induced asymmetries derived from models (Hlywiak & Nolan 2022) or observations (Rogers & Zhang 2023). For example, Figure 1a,b,c demonstrates a systematic weakening of the storm system over the sea (north), which is reflected in the satellite-derived temperatures and SAR-derived wind speed. An almost static reduction in the offshore wind speed, which we coin an 'eyewall break', persisted for over 24 hours. This study aims to investigate previously unexplored environmental mechanisms that could contribute to the asymmetric wind distribution of Tropical Cyclone Veronica.

## 2. DATA AND METHODS

While this study is based on the real case of Tropical Cyclone Veronica (2019), the majority of the data is produced using the Met Office Unified Model in the regional tropical configuration (RA2T) with a 2.2km horizontal resolution. The model is convection-permitting and solves the semi-Lagrangian advective equations for a non-hydrostatic, fully compressible atmosphere (Wood et al. 2014). Figure 1d shows an example of the model performance in reproducing the asymmetry of Veronica. Further model evaluation was performed based on the surface observation sites and is available upon request. Overall, the quality of the MetUM simulation was good.

We also used the boundary layer model of Kepert & Wang (2001) modified by Kepert (2018) to explore the impact of land and local rainband features on the asymmetry of Veronica.

## 3. RESULTS RAINBAND DYNAMICS

Starting by looking at the tangential and radial flow fields of the MetUM simulation during a time of eyewall break (Figure 2), there are several interesting observations to be made. A strong rainband system is associated with the spiral band of outflow in the UR/DR quadrants in Figures 2b,e, suggesting that rainbands can modulate the secondary circulation (which supports the idealised studies of Kepert 2018 and the observational studies of Powell 1990 and Skwira et al. 2005). It seems that the rainband is directing the flow away from the storm centre. This phenomenon is likely caused by strong convergence into the rainband which is exacerbated by the frictional convergence effects of land (not shown). Using storm-centred coordinates, the convergence into the rainband projects as 'outflow', although it can be equally be perceived as inflow into the band. Interestingly, Figure 2e also suggests an east-west throughflow, which extends further than the rainband. Our next results will offer an explanation for the throughflow and for the eyewall break of Veronica (Figures 1c,d and 2a,d), which cannot be explained by the rainband.

It should be noted here that thermodynamic impacts of the rainband (such as radial and downdraft ventilation) were investigated as a potential contributor to the eyewall break. While not shown here, there was no evidence to suggest thermo-

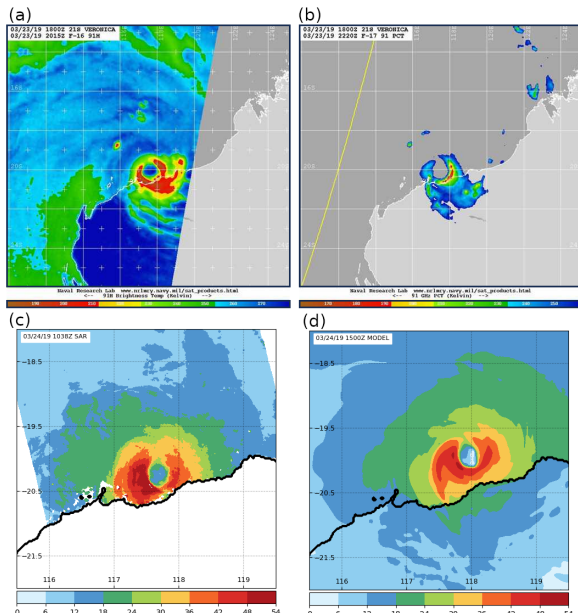


**Figure 1:** (a) Satellite 91 H brightness temperature (K) from the Naval Research Lab on 23 March 2019 20:15 UTC. (b) Satellite 91 GHz polarization-corrected temperature (K) from the Naval Research Lab, on 23 March 2019 22:20 UTC. (c) Satellite-derived SAR 10-m wind speed ( $\text{m s}^{-1}$ ; Mouche et al. 2019) on 24 March 2019 10:38 UTC. (d) Modelled 10-m wind speed ( $\text{m s}^{-1}$ ) on 24 March 2019 15:00 UTC.

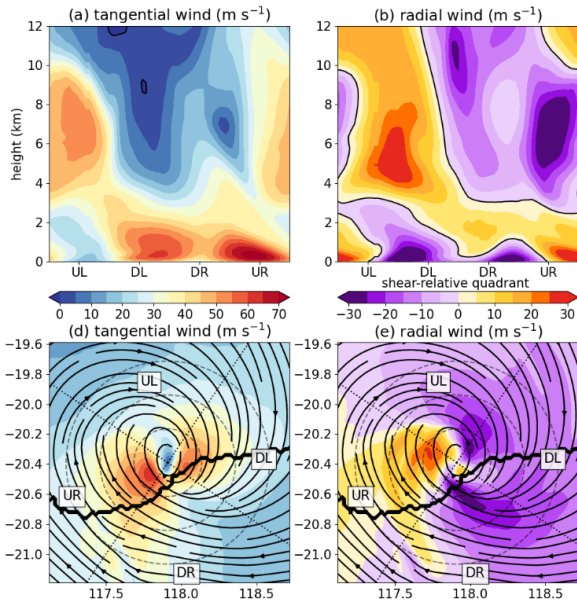


**Figure 2:** (a,b) Cross-sections at the RMW (12 km) for tangential wind ( $\text{m s}^{-1}$ ), radial wind ( $\text{m s}^{-1}$ ) and vertical wind ( $\text{m s}^{-1}$ ) respectively. The unfilled contours denote  $0 \text{ m s}^{-1}$ . (d,e) The same fields as (a,b) but in a plan-view averaged across the lowest 1.5 km. The coastline is shown as a thick black line. Streamlines correspond to the earth-relative wind field. The shear-relative quadrants are labelled as UL: upshear left, DL: downshear left, DR: downshear right, UR: upshear right. Faint dashed circles denote the radius at 25 km intervals. (c,f) have been removed for this abstract.

dynamic depletion over the offshore side of the storm, where the eyewall break is located.

### LARGESCALE VORTICITY

During the analysis, we noticed a largescale gradient of vorticity across Veronica's environment. This is exemplified in Figure 3a,b, where there is more anticyclonic (positive) vorticity in the south and more cyclonic vorticity in the north. If relative vorticity is defined as the curl of the motion vector ( $\nabla \times \vec{V}$ ), then the rotational flow can be reconstructed from the relative vorticity field, following Helmholtz's theorem (Helmholtz 1858). Figures 5a,b show the MetUM vorticity field centred on the eye, and Figure 5d is the total wind speed at 900 hPa in the MetUM. We calculated the rotational flow from the vorticity field (Figure 3e), which demonstrated that the eyewall break of Veronica could be reproduced using the rotational flow component derived from the relative vorticity.

To break this down further, we performed a low-wavenumber (0,1,2) Fourier decomposition of the MetUM vorticity field (Figure 3). Wavenumber-0 (not shown) comprises the symmetric field. Wavenumber-1 (Figure 3b,f) consists of the larger-scale environmental forcing, and wavenumber-2 (Figure 3b,f) explains some of the eyewall ellipticity (e.g. Figure 2d, Figure 3a,b,c,d). Notably, wavenumber-1 shows

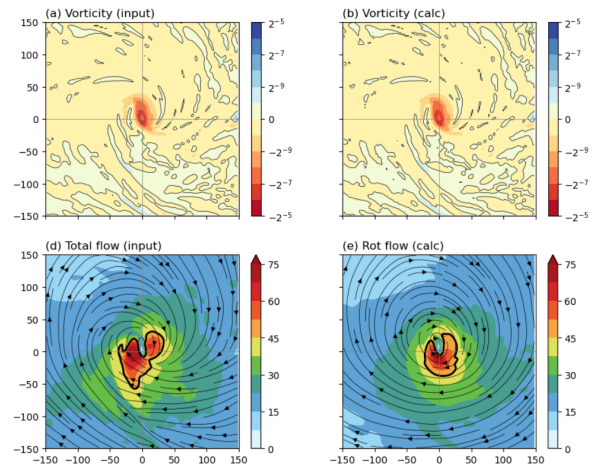


**Figure 3:** (a) Relative vorticity ( $\text{s}^{-1}$ ) input from the MetUM simulations at  $T + 59$ ; 25 September 2019 11:00 UTC. (b) Relative vorticity ( $\text{s}^{-1}$ ) calculated from the wind field in (d). (d) Wind speed (filled;  $\text{m s}^{-1}$ ) and streamlines from the MetUM at the same forecast time as (a), where the thick black contours denote the wind speed at  $45 \text{ m s}^{-1}$ . (e) The rotational flow (filled;  $\text{m s}^{-1}$ ) and associated streamlines, calculated from the vorticity field in (b), where the thick black contours denote the wind speed at  $45 \text{ m s}^{-1}$ . (c,f) have been removed for this abstract.

two largescale gyres of vorticity, reflecting the largescale vorticity gradient in the full field in Figure 3a, whereby there is relatively more cyclonic vorticity in the north and more anticyclonic vorticity in the south. When the wavenumber-1 asymmetry is added to the symmetric wavenumber-0 component (Figure 4f), there is a north-south gradient of vorticity across the storm system.

Informed by the wavenumber-1 component of vorticity from Figure 4 and the vorticity gradient of the MetUM field (calculated as the ratio between the mean vorticity in the southern and northern 150 km of the storm, with the inner 50 km removed), we designed an idealised wavenumber-1 vorticity field (Figure 5b) and added this to a symmetric vorticity field (Figure 5a) from the boundary layer model of Kepert & Wang (2001). Following the earlier logic that the rotational flow can be reconstructed from the vorticity field, Figure 5e shows the rotational flow associated with the vorticity gradient (Figure 5b). The bottom of the cyclonic gyre and the top of the anticyclonic gyre both produce an easterly flow.

When the rotational flow is recalculated using the new vorticity field with the inclusion of the largescale gradient (Figures 5c,f), an eyewall break appears in the north. This is caused by the easterly flow of the anticyclonic and cyclonic features in Figure 5b. This easterly flow impedes the westerly tangential circulation in the north, producing an eyewall break. Conversely, the easterly flow in the south enhances the tangential flow, causing an increase in wind speed. Overall, this

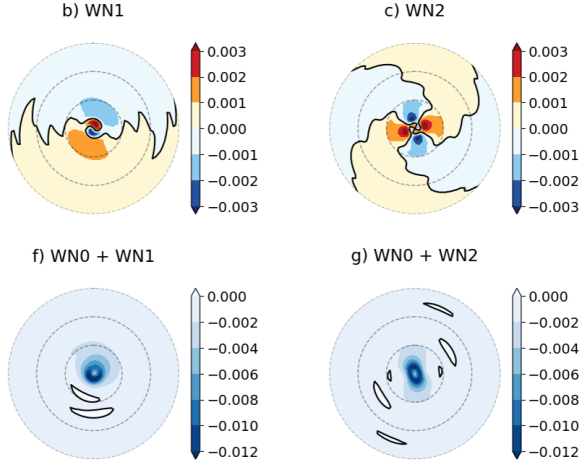


**Figure 4:** Fourier decomposition of the relative vorticity ( $\text{s}^{-1}$ ) at T+59; 25 September 11:00 UTC, during prominent eyewall break (as shown in Figure 3). The top row, (b,c) represent: wavenumber-1, waveumber-2, respectively. The bottom row (f,g) as in (b,c) with the symmetric field (wavenumber-1) included. (a,d,e,h) have been removed for this abstract.

produces an asymmetric wind distribution with a stronger, more expansive wind field in the south. For Veronica, this increased wind speed is over land.

One question that is raised is: how strong does the vorticity gradient need to be to produce an eyewall break? This question is answered in Figure 6, in which we repeated the idealised experiment for a series of vorticity gradients. The magnitude of the eyewall break depends on the relative strength of the symmetric and wavenumber-1 components, reflected by the calculated vorticity gradient which takes into consideration both wavenumber-0 and wavenumber-1. Even a weak vorticity gradient can exert some influence on the asymmetry of the tangential wind.

The calculation of the eyewall break ratio is summarised by the schematic in Figure 7. Taking the minimum and maximum tangential wind along a constant radius would be inappropriate in this case due to the elliptical shape of the eyewall, which would project onto the calculation. Therefore, the methodology is as follows: the maximum tangential wind is taken from each radial around the storm (there are 72 points in our interpolation), with a maximum radius of 150 km from the storm centre. The eyewall break (EWB) is then calculated from the mean ( $\overline{v_{max}}$ ) and minimum ( $\min(v_{max})$ ) of this dataset, taking the form:

$$EWB = \frac{\min v_{max}}{\overline{v_{max}}}. \quad (1)$$

There is an almost perfect positive linear correlation between the eyewall break ratio and the largescale vorticity ( $\zeta$ ) gradient, in our idealised simulations (Figure 8). This is because the result-

ing rotational flow calculated from the idealised vorticity gradient is directly proportional to the strength of the vorticity. Thus, when added to a symmetric storm, the extent of asymmetry can be reliably predicted.

#### 4. DISCUSSION

Although there is a linear relationship between the eyewall break ratio and the vorticity gradient in the idealised simulations (Figure 8), our results showed that the MetUM simulations of Tropical Cyclone Veronica had a stronger eyewall break signal than would be implied by the idealised experiments. The most obvious explanation is that real storms are made up of more components than that of just a symmetric and wavenumber-1, including small-scale features. For example, we showed in Figure 2 that convergence into a strong rainband system contributed to the outward diversion of flow in Veronica, which likely contributed to a reduction in the tangential wind speed in the northern eyewall, increasing the magnitude of the eyewall break.

It can also be recognised now that the east-west throughflow in the radial wind field (Figure 2e) can be at least partially attributed to the largescale vorticity gradient, which exerts an easterly flow to the north and south of the storm centre. This throughflow likely compounded the dynamic impact of the rainband, further diverting the flow away from the storm centre.

We note that the radial and tangential wind fields of Veronica are structurally different to idealised landfalling storms (Hlywiak & Nolan 2022) and observations of a landfalling storm (Rogers & Zhang 2023). These recent studies suggest that landfall induces an inflow maximum in the immediate offshore flow, whereas Veronica exhibited an outflow (Figure 2e). Therefore, we must come to the conclusion that the wind structure of Veronica was not dominated by landfall processes, but was under stronger influence from the spiral rainband and largescale vorticity gradient.

The largescale vorticity gradient seen in Veronica seemed to be produced by the intersection of the monsoon trough in the north and an eastwardly propagating anticyclone in the south of the domain, shown in Figure 9. As demonstrated in the idealised experiments in Figure 6 and Figure 8, the extent of the eyewall break depends on the overall vorticity gradient, which means that a stronger environmental gradient (wavenumber-1) will have more impact on a weaker storm (wavenumber-0). This is important since Veronica experienced a period of weakening during landfall, and the asymmetry became more prominent as the storm weakened.

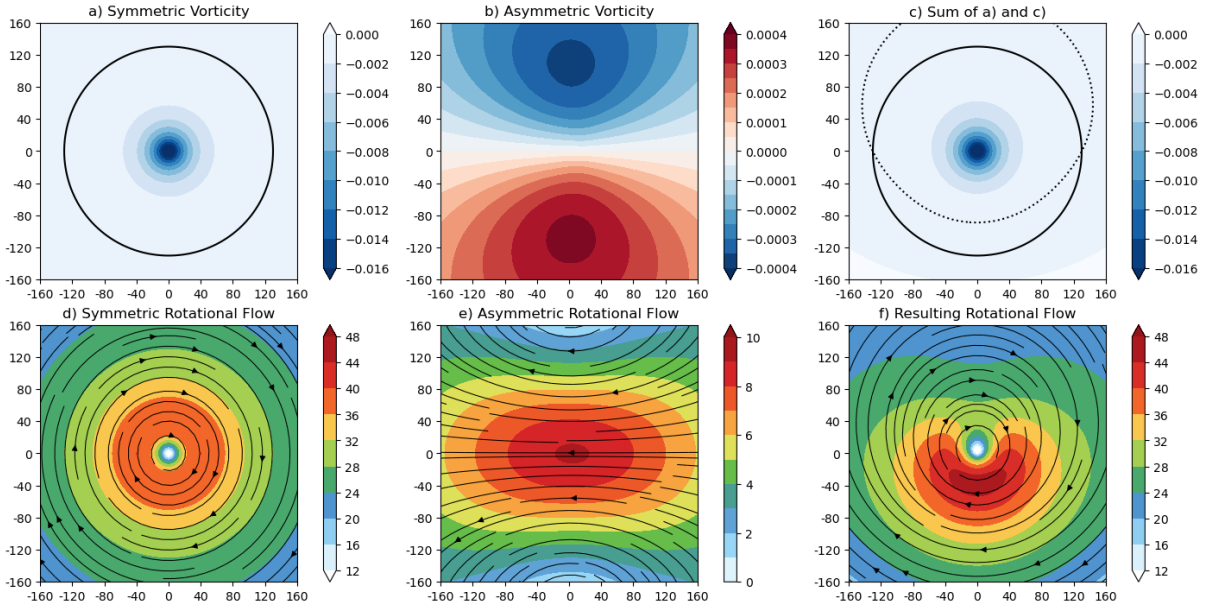


**Figure 5:** (a) Idealised symmetric relative vorticity field ( $\text{s}^{-1}$ ) with a reference contour at  $-0.0005 \text{ s}^{-1}$ . (b) Idealised north-south vorticity gradient ( $\text{s}^{-1}$ ). (c) The sum of (a) and (b) with a reference contour at  $-0.0005 \text{ s}^{-1}$  for (a) (solid) and (c) (dotted). (d) The symmetric rotational flow ( $\text{s}^{-1}$ ) calculated from (a). (e) The rotational flow ( $\text{s}^{-1}$ ) calculated from (b). (f) The rotational flow calculated from (c) ( $\text{s}^{-1}$ ).

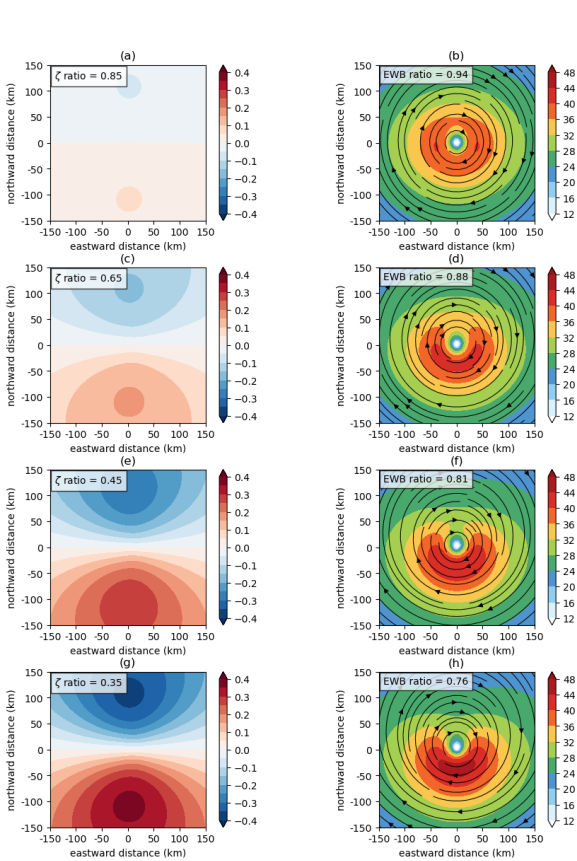


**Figure 6:** (a),(c),(e),(g) Idealised relative vorticity gradients ( $10^{-3} \text{ s}^{-1}$ ) with their overall north-south vorticity ratio annotated. (b),(d),(f),(h) The rotational flow calculated from the asymmetric vorticity field + the symmetric field (e.g. Figure 5c). The eyewall break ratio is annotated. Calculations for the eyewall break ratio and vorticity ratio are described in-text.

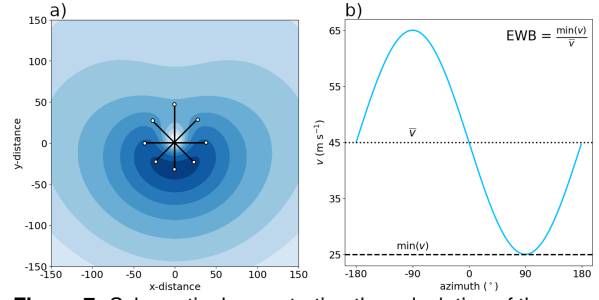


**Figure 7:** Schematic demonstrating the calculation of the eyewall break ratio (EWB). (a) an example asymmetric tangential wind field ( $v$ ; filled). The black lines are radials from the storm centre, with a white circle denoting where the maximum wind is. (b) Idealised asymmetric maximum winds from each radial, plotted by azimuth. The eyewall break ratio is the ratio of the minimum tangential wind ( $\min(v)$ ) to the mean ( $\bar{v}$ ).

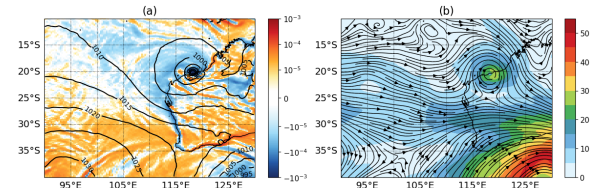


**Figure 9:** MetUM global deterministic forecast at 23 March 2019 00:00 UTC ( $T + 24$ ). (a) Relative vorticity at 850 hPa (filled;  $\text{s}^{-1}$ ), mean sea level pressure (hPa; unfilled contours). (b) Steering-level flow (filled;  $\text{m s}^{-1}$ ) and streamlines.

## 5. CONCLUDING REMARKS

This study highlights the complex dynamics of tropical cyclone. While we use the case study of a landfalling storm, the findings of this work can be applied to tropical cyclone systems anywhere in the world. It is possible that there are multiple mechanisms by which eyewall breaks can be

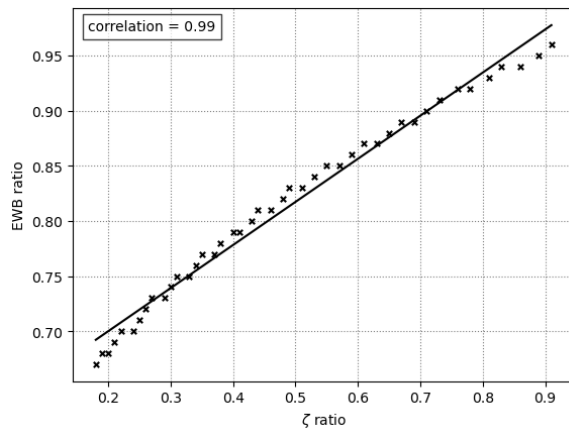


**Figure 8:** Correlation between the north-south relative vorticity gradient ( $\zeta$  ratio) and the eyewall break (EWB) ratio. Correlation coefficient (annotated) is calculated using Pearson's correlation coefficient (Pearson 1901) with a confidence level of  $> 99.9\%$ .

formed, such as thermodynamic depletion (Fischer et al. 2023) or vortex Rossby wave activity (e.g. Reasor et al. 2000, Wang 2002, Corbosiero et al. 2006). However, it is likely that there are many tropical cyclones which experienced an eyewall break due to environmental vorticity gradients. One recent example is Hurricane Idalia (2023), which presented similar tangential wind asymmetries to Veronica, a through-flow in the radial wind, and a consistent vorticity gradient. More work is needed to establish how common it is that tropical cyclone eyewall breaks and asymmetries can be attributed to environmental gradients of vorticity.

There may be broader implications of such asymmetries, which can contribute to intensification or weakening processes in tropical cyclones, and may help to address the progress in predicting intensity change. In this case, we have shown that the vorticity gradient of Tropical Cyclone Veronica (2019) contributed to unexpectedly strong boundary layer winds onshore during landfall, leading to increased risk for coastal communities.

## References

Chan, J. C. & Liang, X. (2003), 'Convective asymmetries associated with tropical cyclone landfall. Part I: f-plane simulations', *Journal of the Atmospheric Sciences* **60**(13), 1560–1576.

Chen, Y. & Yau, M. (2003), 'Asymmetric structures in a simulated landfalling hurricane', *Journal of the Atmospheric Sciences* **60**(18), 2294–2312.

Corbosiero, K. L. & Molinari, J. (2002), 'The effects of vertical wind shear on the distribution of convection in tropical cyclones', *Monthly Weather Review* **130**(8), 2110–2123.

Corbosiero, K. L. & Molinari, J. (2003), 'The Relationship between Storm Motion, Vertical Wind Shear, and Convective Asymmetries in Tropical Cyclones', *Journal of the Atmospheric Sciences* **60**(2), 366–376.

Corbosiero, K. L., Molinari, J., Aiyyer, A. R. & Black, M. L. (2006), 'The Structure and Evolution of Hurricane Elena (1985). Part II: Convective Asymmetries and Evidence for Vortex Rossby Waves', *Monthly Weather Review* **134**(11), 3073–3091.

Fischer, M. S., Reasor, P. D., Tang, B. H., Corbosiero, K. L., Torn, R. D. & Chen, X. (2023), 'A tale of two vortex evolutions: Using a high-resolution ensemble to assess the impacts of ventilation on a tropical cyclone rapid intensification event', *Monthly Weather Review* **151**(1), 297–320.

Helmholtz, H. v. (1858), 'On integrals of the hydrodynamic equations which correspond to the vortex movements.'

Hlywiak, J. & Nolan, D. S. (2022), 'The evolution of asymmetries in the tropical cyclone boundary layer wind field during landfall', *Monthly Weather Review* **150**(3), 529–549.

Kepert, J. D. (2018), 'The boundary layer dynamics of tropical cyclone rainbands', *Journal of the Atmospheric Sciences* **75**(11), 3777–3795.

Kepert, J. & Wang, Y. (2001), 'The dynamics of boundary layer jets within the tropical cyclone core. Part II: Nonlinear enhancement', *Journal of the atmospheric sciences* **58**(17), 2485–2501.

Mouche, A., Chapron, B., Knaff, J., Zhao, Y., Zhang, B. & Combot, C. (2019), 'Copolarized and cross-polarized SAR measurements for high-resolution description of major hurricane wind structures: Application to Irma category 5 hurricane', *Journal of Geophysical Research: Oceans* **124**(6), 3905–3922.

Pearson, K. (1901), 'On the Lines and Planes of Closest Fit to Systems of Points in Space', *Philosophical Magazine* **2**(11), 559–572.

Powell, M. D. (1990), 'Boundary Layer Structure and Dynamics in Outer Hurricane Rainbands. Part I: Mesoscale Rainfall and Kinematic Structure', *Monthly Weather Review* **118**(4), 891–917.

Reasor, P. D., Montgomery, M. T., Marks, F. D. & Gamache, J. F. (2000), 'Low-wavenumber structure and evolution of the hurricane inner

- core observed by airborne dual-Doppler radar', *Monthly Weather Review* **128**(6), 1653–1680.
- Rogers, R. F. & Zhang, J. A. (2023), 'Airborne Doppler radar observations of tropical cyclone boundary layer kinematic structure and evolution during landfall', *Geophysical Research Letters* **50**(23), e2023GL105548.
- Shimada, U., Reasor, P. D., Rogers, R. F., Fischer, M. S., Marks, F. D., Zawislak, J. A. & Zhang, J. A. (2024), 'Shear-Relative Asymmetric Kinematic Characteristics of Intensifying Hurricanes as Observed by Airborne Doppler Radar', *Monthly Weather Review* **152**(2), 491–512.
- Skwira, G. D., Schroeder, J. & Peterson, R. E. (2005), 'Surface observations of landfalling hurricane rainbands', *Monthly weather review* **133**(2), 454–465.
- Uhlhorn, E. W., Klotz, B. W., Vukicevic, T., Reasor, P. D. & Rogers, R. F. (2014), 'Observed hurricane wind speed asymmetries and relationships to motion and environmental shear', *Monthly Weather Review* **142**(3), 1290–1311.
- Wang, Y. (2002), 'Vortex Rossby waves in a numerically simulated tropical cyclone. Part II: The role in tropical cyclone structure and intensity changes', *Journal of the atmospheric sciences* **59**(7), 1239–1262.
- Wood, N., Staniforth, A., White, A., Allen, T., Diamantakis, M., Gross, M., Melvin, T., Smith, C., Vosper, S., Zerroukat, M. et al. (2014), 'An inherently mass-conserving semi-implicit semi-Lagrangian discretization of the deep-atmosphere global non-hydrostatic equations', *Quarterly Journal of the Royal Meteorological Society* **140**(682), 1505–1520.